

# Wavelength- and alignment-dependent photoionization of N<sub>2</sub> and O<sub>2</sub>

Simon Petretti, Álvaro Magaña, and Alejandro Saenz

*AG Moderne Optik, Institut für Physik, Humboldt-Universität zu Berlin, Newtonstrasse 15, D-12489 Berlin, Germany*

Piero Decleva

*Dipartimento di Scienze Chimiche e Farmaceutiche, Università di Trieste, Via L. Giorgieri 1, I-34127 Trieste, Italy*

(Received 11 March 2016; published 14 November 2016)

The ionization behavior of the two diatomic molecules nitrogen and oxygen in strong laser fields has been investigated. For this purpose, the time-dependent Schrödinger equation is solved numerically within the many-electron single-determinant approximation. Three different orientations of the molecular axis with respect to the laser field have been considered: 0°, 45°, and 90°. The photon wavelength has been varied from 25 to 800 nm, covering a range from XUV to infrared radiation. Nitrogen and oxygen were chosen as they possess the same molecular symmetry but different orbital structures. The ionization from different orbitals is discussed.

DOI: [10.1103/PhysRevA.94.053411](https://doi.org/10.1103/PhysRevA.94.053411)

## I. INTRODUCTION

One of the goals in strong-field physics is the time-resolved imaging of fast structural changes or chemical reactions. If long wavelengths and high intensities are adopted, it is often assumed that ionization can well be described by tunneling. In this case, the ionization probability depends exponentially on the electrons' binding energies. Thus, ionization may dominantly occur from the most loosely bound orbital, the chemically active highest-occupied molecular orbital (HOMO). Since also molecular structure (nodes, etc.) plays a role, the HOMO may be “imaged” by observing the ionization probability as a function of the relative orientation of the laser polarization axis and the molecule [1–3]. Based on the famous three-step model of high-harmonic generation (tunnel ionization, field-driven propagation, return to the parent ion) also the emitted harmonics [4] or the scattered electrons [5] may provide time-resolved structural information.

A much more direct imaging of the electronic structure is, on the other hand, possible when adopting short wavelengths since then the final state is much closer to a simple Coulomb or even a plane wave. Therefore, in a previous work the strong-field response of H<sub>2</sub> had been investigated theoretically [6] covering the wavelength range from 50 to 400 nm. However, it is well known that radiation of shorter wavelengths preferentially probes inner orbitals. Since the wavelengths available at most of the free-electron lasers are in the intermediate energy regime of the XUV, it is of course interesting to have a more quantitative estimate of the relative importance of the different orbitals. We have thus investigated the role of the different orbitals in the ionization of N<sub>2</sub> and O<sub>2</sub> when varying the wavelength (and alignment angle) in between 800 and 25 nm and thus covering the range from the titan sapphire lasers to, e.g., FLASH in Hamburg or FERMI in Trieste.

## II. METHOD

The method employed was introduced earlier in Refs. [2,3,7,8]. To recall, the nonrelativistic approximation is used, and the laser-electron interaction is treated semi-classically within the dipole approximation. The field-free

time-independent molecular electronic structure is described quantum mechanically in the Born-Oppenheimer approximation. The time-dependent Schrödinger equation (TDSE) is then solved numerically in the basis of field-free eigenstates.

A time-independent density-functional theory (DFT) field-free Hamiltonian is employed

$$H^0 = \sum_i h_{KS}(i), \quad h_{KS} = -\frac{1}{2}\Delta + V_N + V_C + V_{XC}, \quad (1)$$

which is completely defined by the ground-state density, obtained from a preliminary self-consistent field calculation employing the ADF quantum chemistry program.  $V_N$  is the nuclear potential, and  $V_C$  is the Coulomb potential generated by the charge density. For the exchange-correlation potential  $V_{XC}$  the LB94 potential [9] has been employed as it gives a balanced description of both ground and excited states. The Kohn-Sham Hamiltonian  $h_{KS}$  is then diagonalized in a new symmetry-adapted basis set, built from products of radial  $B$  splines times real spherical harmonics. It is composed by one set used to describe a large central sphere (with a radius of  $r_{\max}^0$ ) and additional sets used to build (nonoverlapping) atom-centered spheres [10] to efficiently describe the Coulomb cusps of the wave function. This linear combination of atomic orbitals  $B$ -spline basis is effectively complete within the sphere of radius  $r_{\max}^0$  and can describe very accurately the propagation of the wave packet provided it does not reach the outer boundary.

Starting from the ground-state configuration,

$$|\Phi_0\rangle = |\varphi_1 \cdots \varphi_n\rangle, \quad (2)$$

at  $t = 0$  with the field-free Kohn-Sham orbitals  $|\varphi_j\rangle$ , this many-electron wave function is time propagated under the electric dipole perturbation, yielding  $n$  independent equations which are solved in the spectral basis of eigenstates  $|\varphi_j\rangle$  of  $h_{KS}$ , requiring only the eigenenergies and dipole matrix elements of the unperturbed molecule. The expansion coefficient  $c_j$  of the active orbital (the orbital that is time propagated) is set to one at  $t = 0$ . In contrast to a standard frozen-core approach (method A in Ref. [2]) we include all orbitals in the expansion of the total wave function as the orbitals remain orthogonal under the unitary evolution of the time-dependent Hamiltonian. We

refer to this procedure that was demonstrated to be gauge invariant and to obey the Pauli principle at all times as the many-electron single-determinant (MESD) approximation (method B in Ref. [2]). The approach is not identical to time-dependent density-functional theory. As the time-dependent change in the potential due to the field is neglected, the MESD is expected to be valid only if ionization, and thus a change in the electron density, is very small. Noteworthy, within this approximation the individual propagation of the active orbitals, i.e., one independent TDSE calculation per active orbital, is fully identical to the result obtained if the complete Slater determinant would be propagated. After the time propagation of the active orbital  $|\varphi_j\rangle$  the ionization (or electron) yield  $Y_j$  for orbital  $j$  that possesses in the initial-state configuration the occupation number  $d_j$  is obtained as

$$Y_j = d_j \sum_{k>k_{\text{th}}} |c_k(t=T)|^2, \quad (3)$$

where the sum extends only over the (discretized) continuum orbitals ( $k_{\text{th}}$  is the index of the highest-lying bound orbital) and  $T$  is the pulse duration. Note that, in the case of degenerate orbitals, each of the components contributes separately. For example, in the case of a fully occupied  $1\pi_u$  orbital, the contributions from the  $1\pi_{u,x}$  and the  $1\pi_{u,y}$  orbitals are summed to give  $Y_{1\pi_u}$ . The total electron yield  $Y_{\text{tot}}$  is here defined as the sum of the ionization yields  $Y_j$  of all individual active orbitals that are occupied in the initial-state configuration,

$$Y_{\text{tot}} = \sum_{j=1}^{n_{\text{occ}}} Y_j. \quad (4)$$

Both Eqs. (3) and (4) evidently allow for yields larger than one due to multiple ionization. As it is not expected that the here adopted model provides a good approximation for multiple ionizations in intense laser fields, in the present paper the laser parameters were chosen in a way that the total electron yields  $Y_{\text{tot}}$  remain below one. In the considered cases the ionization yields from single orbitals are less than 0.2 (mostly much smaller). Thus the shown total electron yields, corresponding to a first-order expansion of the determinant into singly excited configurations from the ground-state configuration, should be a reasonably good approximation for the yield of singly charged ions. In Ref. [7] it was in fact shown that at least for molecular hydrogen for which a comparison to a full two-electron calculation is possible, Eq. (3) provides a very good approximation for the yield of singly charged ions if its value is below about 0.1–0.2.

The respective time-propagation calculations are all performed in the length gauge and adopting a cosine-squared shaped pulse with a peak intensity of  $1 \times 10^{13}$  W/cm<sup>2</sup> and a duration of 30 cycles. The field-free electronic structure of N<sub>2</sub> (O<sub>2</sub>) is calculated for the experimentally determined equilibrium geometry  $R_e = 2.068$  atomic units (a.u.) ( $R_e = 2.28$  a.u.) [11].

### III. CONVERGENCE STUDY

As it is only possible to adopt a finite basis set in the calculation, its convergence has to be checked. In the present TDSE calculations the most critical issues are the parameters

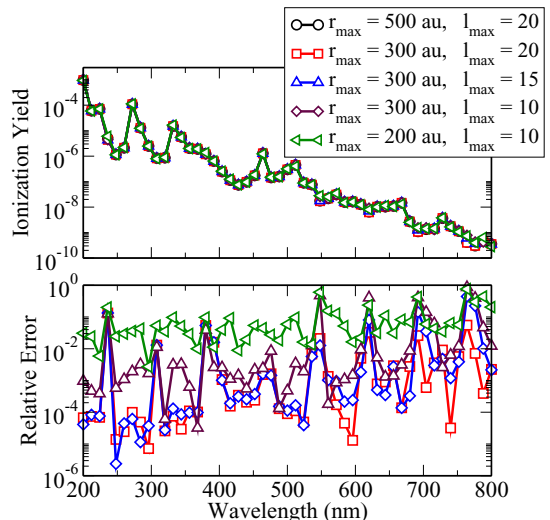


FIG. 1. The orbital ionization yield  $Y_{3\sigma_g}$  of N<sub>2</sub> as a function of the laser wavelength for a parallel alignment with respect to the pulse polarization is shown for different basis sets (upper plot). The corresponding relative error with respect to the reference calculation (box size  $r_{\text{max}}^0 = 500$  a.u., 1019  $B$  splines, and  $l_{\text{max}} = 20$ ) is shown in the lower graph. The pulse is  $\cos^2$  shaped, has a peak intensity of  $1 \times 10^{13}$  W/cm<sup>2</sup>, and a duration of 30 cycles.

of the central  $B$ -spline basis, namely, the box-size (sphere radius)  $r_{\text{max}}^0$ , the number of  $B$  splines, and the maximum angular momentum  $l_{\text{max}}$  of the spherical-harmonics expansion. The box size determines the range in which the wave packet can be described, and a too small box leads to unphysical reflections at the box boundary. Since the quiver-motion radius of an electron in a laser field scales proportional to the square of the laser wavelength, the box size has to be larger for long-wavelength radiation. The  $B$ -spline density (the number of  $B$  splines divided by the box size) determines the largest electron momentum that can be described. Finally, an increasing number of absorbed photons is connected to an increasing angular momentum, and thus one expects that again more angular momenta have to be included for longer wavelengths if similar laser durations and peak intensities are considered.

An example of the convergence behavior is shown in Fig. 1. The electron yield (ionization yield) for the  $3\sigma_g$  orbital of N<sub>2</sub> and for an alignment angle of  $\theta = 0$  (parallel orientation) is shown as a function of the laser wavelength between 200 and 800 nm for a number of basis sets. The calculations all adopt a  $\cos^2$  laser pulse with a 30-cycle pulse duration and a peak intensity of  $1 \times 10^{13}$  W/cm<sup>2</sup>. For the cases shown in Fig. 1 the box sizes vary between 200 and 500 a.u., and the included angular momenta of the spherical harmonics vary between 10 and 20. The number of  $B$  splines was kept constant at 1019  $B$ -spline functions leading to a correspondingly changing  $B$ -spline density. On the scale of the graph, practically all curves agree with each other. Declaring the result with the largest box  $r_{\text{max}}^0 = 500$  a.u. and the largest number of spherical-harmonics angular momenta  $l = 20$  as a reference, the relative deviations of the results obtained for the other basis sets are shown in the bottom of Fig. 1. The

TABLE I. Ionization potentials  $I_p$  of the relevant HOMOs of  $N_2$  as obtained within the DFT approach and the experimental data obtained by Baltzer *et al.* [16]. The corresponding  $N$ -photon ionization thresholds (values rounded) are listed from one to five photons. For the HOMO  $3\sigma_3$  and the HOMO-1  $1\pi_u$ , these are shown by vertical lines in Fig. 2.

Orbital	$I_p$ (eV)	Reference [16]	$N$ -photon ionization threshold (nm)				
			1	2	3	4	5
$3\sigma_g$	15.9	15.9	78	156	234	311	389
$1\pi_u$	17.5	16.9	71	141	212	283	354
$2\sigma_u$	19.0	18.8	65	130	196	261	326
$2\sigma_g$	33.1	28.8	37	75	112	150	187

results indicate that the (nondifferential) ionization yield is less sensitive to the basis parameters than one may possibly expect from an estimate of the quiver radius or the number of photons that has to be absorbed until the ionization threshold can be reached. Although an energy-resolved electron spectrum may (on a logarithmic scale) be strongly distorted by reflections at the box boundary, the integrated spectrum can still be reasonable. Similarly, in a linear-polarized laser field the angular momentum may increase or decrease in every dipole transition. Therefore, a smaller than expected number of angular momenta can lead to sufficiently accurate results. This is different in circularly polarized light where the absolute value of the angular momentum strictly increases with every dipole transition, which makes this case computationally much more demanding.

As it is the purpose of this paper to illustrate the overall wavelength dependence of the ionization from different orbitals, it is concluded from the convergence studies that, in the case of  $N_2$  ( $O_2$ ) the box size of  $r_{\max}^0 = 200.35$  a.u. ( $r_{\max}^0 = 160.00$  a.u.), the maximum number of angular momenta  $l_{\max} = 10$  ( $l_{\max} = 12$ ) and the energy cutoff parameter 10 a.u. are sufficient. For the alignment-dependent calculations we found out that it is sufficient to include symmetries up to  $\Lambda = 6$  for getting converged orbital ionization yields.

#### IV. RESULTS

From the experimental investigation of the ionization behavior at 800 nm it is known that the ionization yield is largest if  $N_2$  is aligned parallel and  $O_2$  is aligned at  $45^\circ$  [1]. The reason for this result was explained by the orbital structures of the respective HOMOs. Meanwhile, however, several works have shown that there can be contributions to the ionization yield from lower-lying orbitals (HOMO- $X$ ), depending on the orientation [8, 12–14].

TABLE II. The same as in Table I but for  $O_2$ . The experimental ionization potentials [17, 18] are taken as the average between doublet and quartet final states. For the HOMO  $1\pi_g$  and the HOMO-1  $1\pi_u$   $N$ -photon ionization thresholds are shown by vertical lines in Fig. 3.

Orbital	$I_p$ (eV)	References (Expt.)	$N$ -photon ionization threshold (nm)				
			1	2	3	4	5
$1\pi_g$	12.5	12.3 [17]	99	198	298	397	496
$1\pi_u$	19.2	17 [17]	65	129	193	258	322
$3\sigma_g$	19.5	19 [17]	64	127	191	255	318
$2\sigma_u$	25.8	26 [17]	48	96	144	192	241
$2\sigma_g$	37.9	40.6 [18]	33	65	98	131	163

In this paper we explore the behavior of the ionization yield ( $Y_j$ ) for the three orientations, parallel, perpendicular, and  $45^\circ$  over a range of incident photon wavelengths from the usual Ti:sapphire 800 nm (1.55 eV) down to 25 nm (49.6 eV), i.e., all the way into the VUV regime of interest in free-electron laser studies. The rather modest intensity of  $1 \times 10^{13}$  W/cm<sup>2</sup> has been chosen in order to avoid saturation for the shortest wavelengths. This choice of intensity puts the whole range explored within the limits of the so-called multiphoton regime and ensures the validity of the dipole approximation employed in the TDSE. Following, e.g., Reiss [15] the ponderomotive force is  $U_p = 0.6$  eV at 800 nm (Keldysh parameter  $\gamma = 3.2$ ) with  $z = U_p/\omega = 0.4$ , and thus at the border of the perturbative region, whereas already at 200 nm, it is  $U_p = 0.04$  eV ( $\gamma = 13$ ) and  $z = 0.006$ . In the whole region  $U_p \ll I_p$ . Nevertheless, for the longest wavelengths considered, a borderline regime should be reached where the tunneling picture starts to be visible.

For a better resolution of the peak structure in the energy domain we set the number of cycles to 30 (see, for example, the comparison of 10- and 30-cycle pulses in Ref. [6] for  $H_2$ ). The ionization-wavelength spectra for  $N_2$  and  $O_2$  discussed below contain some common features, such as the occurrence of resonance-enhanced multiphoton ionization (REMPI) peaks. A certain number of photons  $n$  is required to reach an excited state from which the absorption of  $q$  photons leads to ionization. This is then called a  $(n + q)$ -REMPI. Such REMPI peaks can be identified straightforwardly by analyzing the energy positions and the corresponding excitation yields (see below).

Other common features are the channel closings that occur whenever the photon energy or a multiple of it is no longer sufficient to overcome the ionization potential of the active orbital. At these energies the ionization yield then usually drops by some orders of magnitude, whereas the excitation yield increases drastically due to population of the Rydberg

TABLE III. Further ionization potentials  $I_p$  for  $N_2$  and  $O_2$  (as obtained within the DFT approach) which are helpful for the determination of resonant structures in Figs. 2 and 3.

Orbital	$I_p$ (eV)	
	$N_2$	$O_2$
$4\sigma_g$	3.50	3.80
$5\sigma_g$	1.40	1.35
$3\sigma_u$	2.47	3.44
$4\sigma_u$		1.47
$1\pi_g$	8.04	12.49
$2\pi_g$	1.00	1.05
$3\pi_g$		0.67
$2\pi_u$	2.45	2.35
$3\pi_u$	0.90	0.98
$1\delta_g$	1.07	1.02

states (cf. Ref. [6]). In Tables I and II the ionization potentials of the relevant HOMO- $X$  orbitals and the wavelengths defining the  $N$ -photon ionization thresholds up to  $N = 5$  are explicitly given for  $N_2$  and  $O_2$ , respectively. For example, for the HOMO  $3\sigma_g$  of  $N_2$  in Table I up to 78 nm one photon is sufficient for ionization, whereas in between 234 and 311 nm, four photons are necessary for ionization.

In comparison with  $N_2$ , in  $O_2$  there are two more electrons that occupy the next molecular orbital  $1\pi_g$ , decreasing the HOMO  $I_p$ , whereas all remaining orbitals are shifted to higher energy because of increased nuclear attraction. Therefore, the HOMO of  $N_2$  correlates with the HOMO-2 in  $O_2$  (because of orbital switching) whereas the HOMO-1 is  $1\pi_u$  in both molecules. Some low-lying virtual-state energies are also reported in Table III as a help to understand the resonant peak positions.

As is also evident from a comparison of the calculated orbital energies with the experimental ones (see Table I for  $N_2$  and Table II for  $O_2$ ), DFT eigenvalues obtained with the LB94 functional are only a fair approximation of the experimental ionization potentials. Due to the survey nature of this paper we also neglected spin coupling in the case of  $O_2$ . Thus, ionization is considered at the single-particle level as an average of the spin-multiplet final states. The same applies to the innermost  $2\sigma_g$  ionization, which is in fact split by many-body effects. Again, the LB94 values are a fair approximation for those averages.

In Fig. 2 the ionization yields of  $N_2$  for the relevant occupied orbitals are shown as a function of the incident photon wavelength for the three alignment angles  $0^\circ$ ,  $45^\circ$ , and  $90^\circ$  from top to bottom and likewise in Fig. 3 for  $O_2$ . The  $N$ -photon ionization thresholds are marked as vertical lines in Figs. 2 and 3 for the HOMO (solid red lines) and HOMO-1 (dashed blue lines) of  $N_2$  and  $O_2$ . Also the main resonant excitations are indicated for the ionizations from each of the three outermost orbitals.

Several general trends are readily apparent in the spectrum of  $N_2$  in Fig. 2.

(1) For the same intensity and pulse duration,  $Y_j$  increases steadily with increasing photon energy. Some steps indicating the  $N$ -photon thresholds are visible, but only those corresponding to the few-photon cases, such as the thresholds

for  $N = 1-3$  in the case of the HOMO, despite the rather narrow bandwidth of the pulse (about  $\Delta\omega/\omega = 1\%$ ). For the HOMO-1, the visibility of the thresholds extends to longer wavelengths. The general disappearance of the thresholds with increasing wavelength and for lower  $I_p$  indicates the expected breakdown of lowest-order perturbation theory. The global slope of  $Y_j$  is not too different for HOMO, HOMO-1, and HOMO-2 (their  $I_p$ 's lie within 3 eV), whereas it is much higher for the HOMO-3, which is much more deeply bound, and its ionization is basically suppressed up to 200 nm. Then the ion yield increases steeply, becoming of the same order of magnitude as the one of the other orbitals around 70 nm and again at 25 nm. Although masked by irregular behavior, some correlation between the increasing  $I_p$  and the slope appears also for the outer valence orbitals.

(2) While in the lower photon-energy range the HOMO ionization is often dominant (with the exception of HOMO-1 in the range of 800–700 nm for the perpendicular and the  $45^\circ$  orientation), the situation changes drastically already at about 400 nm. There is a frequent exchange of dominant ionization, associated with very structured profiles of  $Y_j$ , notably a huge resonance in the  $1\pi_u$  channel around 130 nm (associated with the  $1\pi_u \rightarrow 1\pi_g$  excitation) in the parallel orientation and a similar resonance in the  $2\sigma_u$  channel in the perpendicular orientation, again associated with the strong  $2\sigma_u \rightarrow 1\pi_g$  excitation. Finally, even at the lower photon energies,  $Y_j$  does not always follow the inverse  $I_p$  ordering. In fact, for the parallel orientation, ionization of the inner  $2\sigma_u$  orbital is consistently higher than that from the higher-lying  $1\pi_u$ , over the extended wavelength range of 800–400 nm.

(3) A lot of structure is present in all  $Y_j$  profiles due to REMPI processes, which is relatively weak at the longest wavelengths but becomes progressively sharper and more pronounced at higher photon energies, in line with the increasing multiphoton character of the ionization due to the availability of strong intravalence transitions to low-lying states. In particular the sharpest structures appear to be associated with the innermost  $2\sigma_g$  orbital, suggesting an increase in the multiphoton character of its ionization, which can be justified by the reduced role of tunneling associated with its high  $I_p$ .

The ionization yield for  $O_2$  is reported in Fig. 3. Most of the trends observed in  $N_2$  are also found here with some new features. In this case, because of the large  $I_p$  gap between HOMO and HOMO-1, the HOMO  $1\pi_g$   $Y_j$  is largely dominant from 800 nm up to about 200 nm, and even at shorter wavelengths it remains dominant, especially for the parallel orientation, with the exception of the narrow regions just below 200 nm where it is overtaken by  $1\pi_u$  ionization because of a broad REMPI  $1\pi_u \rightarrow 1\pi_g$  resonance and between 110 and 130 nm where there is a jump in the  $3\sigma_g$   $Y_j$  (possibly  $3\sigma_g \rightarrow 3\sigma_u$  resonance or opening of the two-photon threshold). The situation changes for  $45^\circ$  and  $90^\circ$  orientations where there is a lot of competition below about 65 nm, the opening of one-photon ionization for  $1\pi_u$  and  $3\sigma_g$  since all orbitals lead to ionization of comparable intensity.

The close  $I_p$  values of the  $1\pi_u$  (now HOMO-1) and the  $3\sigma_g$  are reflected in quite similar ionization yields. However, the  $3\sigma_g$   $Y_j$  is in general larger for parallel orientation, whereas the  $1\pi_u$   $Y_j$  dominates in the perpendicular case with a continual

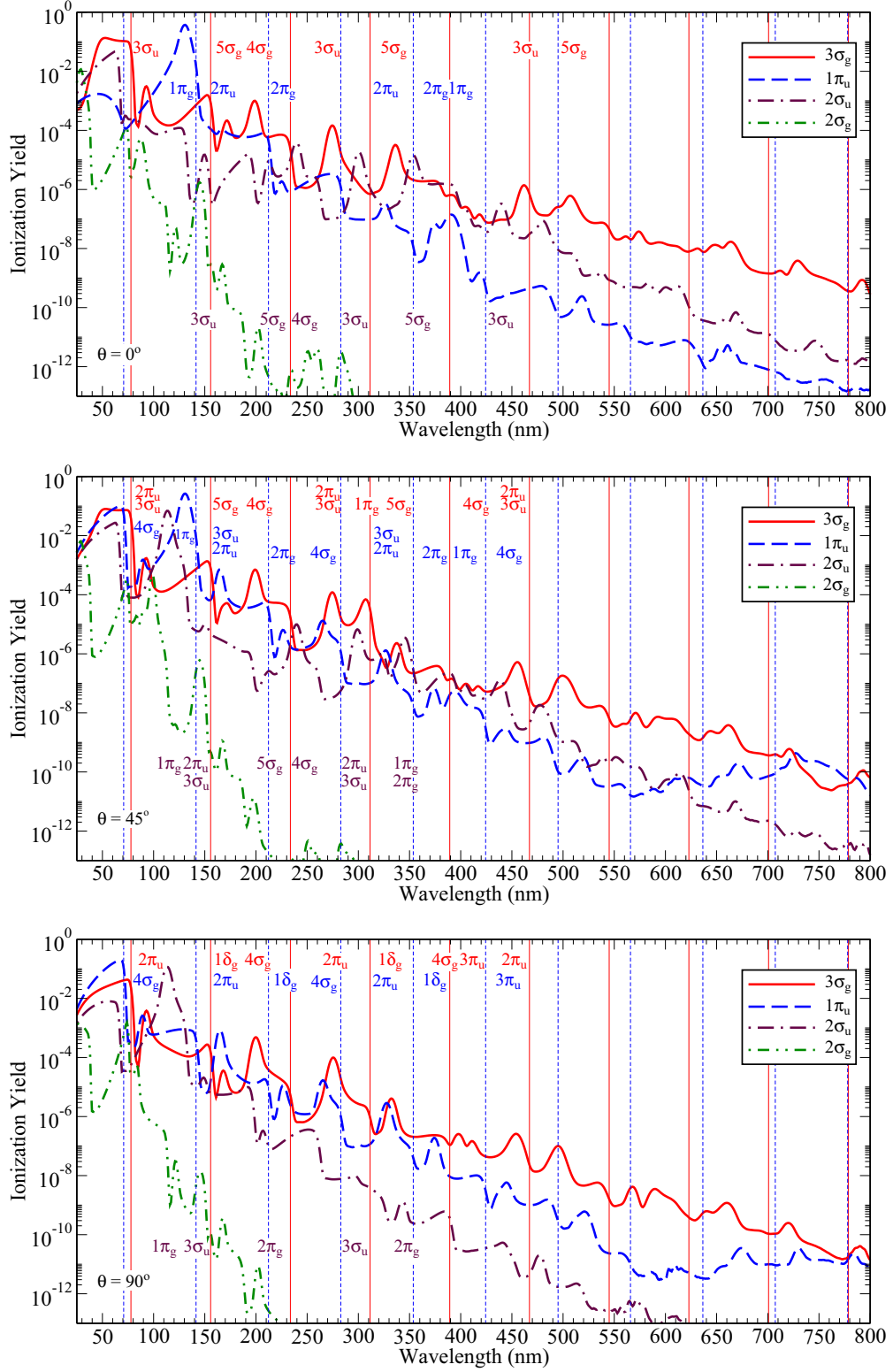


FIG. 2. Orbital ionization yields  $Y_j$  as defined in Eq. (3) of molecular nitrogen as a function of the photon wavelength for the three alignment angles  $\theta = 0^\circ$ ,  $45^\circ$ , and  $90^\circ$  (from top to bottom). The active orbitals are the HOMO  $3\sigma_g$  (red lines), the HOMO-1  $1\pi_u$  (blue lines), the HOMO-2  $2\sigma_u$  (maroon lines), and the HOMO-3  $2\sigma_g$  (green lines). In each case, a  $\cos^2$  laser pulse with a 30-cycle pulse duration is used, and the laser peak intensity is  $1 \times 10^{13}$  W/cm $^2$ . The vertical solid red lines mark the  $N$ -photon ionization threshold for the HOMO  $3\sigma_g$ , whereas the dashed blue ones visualize those of the HOMO-1  $1\pi_u$ . For clarity, the  $N$ -photon thresholds for the other orbitals are not shown but are listed in Table I. The main resonant excitations are indicated for the ionizations from each of the three outermost orbitals.

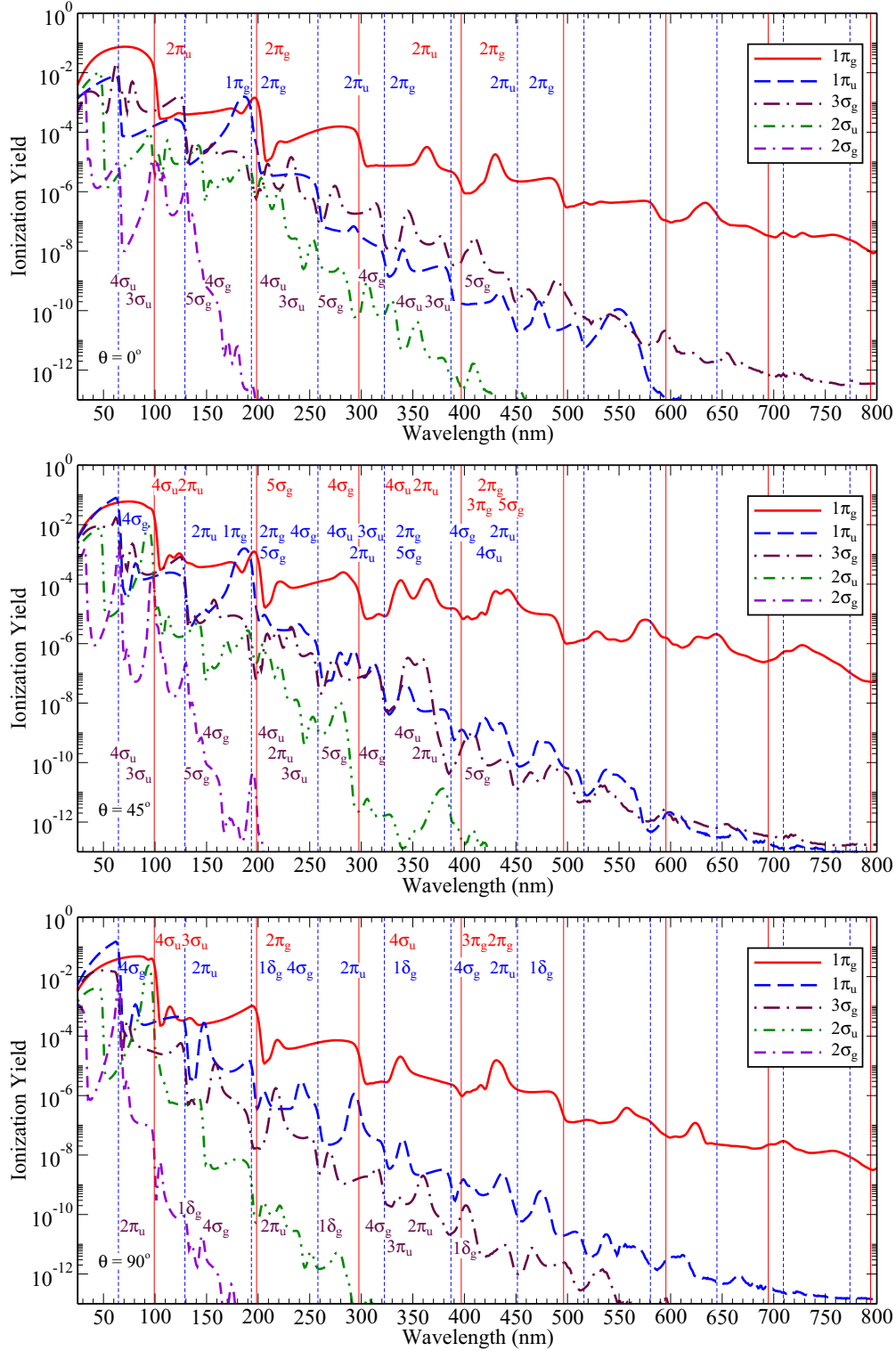


FIG. 3. As Fig. 2 but for molecular oxygen. The active orbitals are the HOMO  $1\pi_g$  (red lines), the HOMO-1  $1\pi_u$  (blue lines), the HOMO-2  $3\sigma_g$  (maroon lines), the HOMO-3  $2\sigma_u$  (green lines), and the HOMO-4  $2\sigma_g$  (violet lines). The vertical solid red lines mark the  $N$ -photon ionization threshold for the HOMO  $1\pi_g$ , whereas the dashed blue ones visualize those of the HOMO-1  $1\pi_u$ . For clarity, the  $N$ -photon thresholds for the other orbitals are not shown but are listed in Table II.

interchange observed at  $45^\circ$ . The large energy gap with the following  $2\sigma_u$  and  $2\sigma_g$  ionizations sets their ionization yields far apart, and their general profiles are much steeper so that they come into play at around 100 nm. Again, on top of the

general trends strong REMPI resonances are superimposed which become sharper for the deeper-lying orbitals. Extreme cases are seen in the resonance in  $2\sigma_u$  around 80 nm or in  $2\sigma_g$  at 100 and 65 nm, which appear particularly sharp at  $45^\circ$ ,

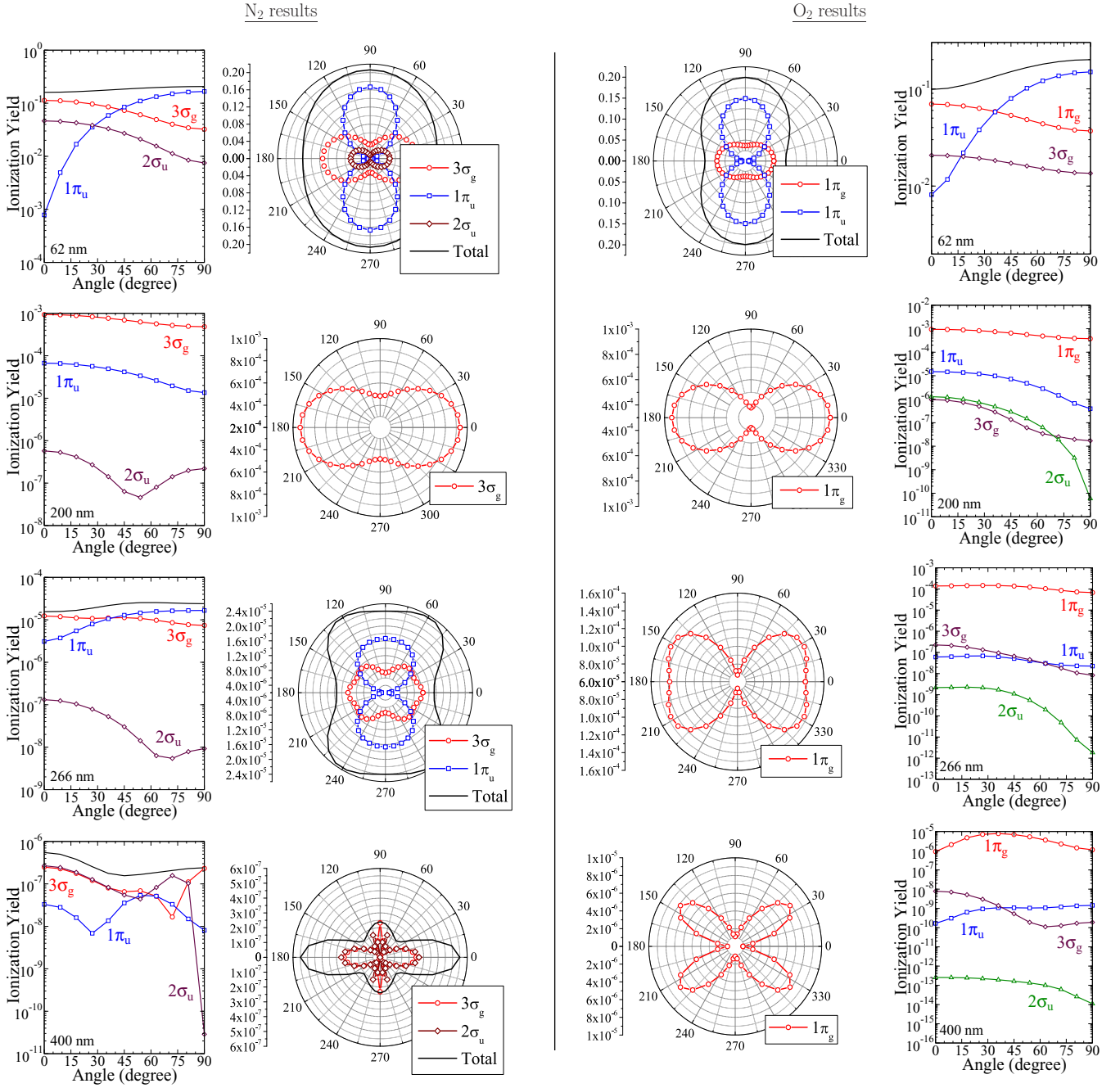


FIG. 4. Variation of the orbital ionization yields with the alignment angle for different wavelengths (62, 200, 266, and 400 nm from top to bottom) and the peak intensity  $1 \times 10^{13}$  W/cm<sup>2</sup> for nitrogen (left) and oxygen (right). For N<sub>2</sub> the contributing orbitals are the HOMO  $3\sigma_g$  (red lines), the HOMO-1  $1\pi_u$  (blue lines), and the HOMO-2  $2\sigma_u$  (maroon lines) and for O<sub>2</sub> the HOMO  $1\pi_g$  (red lines), the HOMO-1  $1\pi_u$  (blue lines), the HOMO-2  $3\sigma_g$  (maroon lines), and the HOMO-3  $2\sigma_u$  (green lines). The smooth (black) lines denote the total electron yields  $Y_{\text{tot}}$  as defined in Eq. (4), which we have omitted for clarity in the plots where the contribution of only one orbital dominates the entire angular region.

and increase  $Y_j$  by about three orders of magnitude. Although very small in absolute magnitude, also the sharp resonance at 200 nm in  $2\sigma_g$  is notable as it does not show either at parallel or perpendicular orientations, suggesting the presence of two resonant intermediate states of different azimuthal quantum numbers, such as a  $2\sigma_g \rightarrow 3\sigma_u \rightarrow 1\pi_g \rightarrow \dots$  excitation. It is generally true that at 45°  $Y_j$  shows a more resonant structure than either at 0° or at 90°.

A selection of full angular scans is reported in Fig. 4 for N<sub>2</sub> and O<sub>2</sub> at 62, 200, 260, and 400 nm (20, 6.2, 4.65 and 3.1 eV) photon energies. At 20 eV the one-photon channel is open, and in both molecules there is a crossing between HOMO ionization, which is dominant in the parallel orientation and that from HOMO-1  $1\pi_u$ , which dominates at 90°. Whereas the shape of the  $Y_j$  angular dependence for the  $1\pi_u$  is very similar, the one for the HOMO is significantly different, being

much broader in  $O_2$ . Actually, it is less different than could be expected on the basis of the shapes of the HOMO orbitals, which is very different for  $N_2$  ( $3\sigma_g$ ) and  $O_2$  ( $1\pi_g$ ). In fact, the characteristic four-lobe structure expected at long wavelengths for the  $1\pi_g$  [1,2,19,20] starts appearing at longer wavelengths, at 266 nm, and becomes fully developed at 400 nm. In  $O_2$ , below the one-photon threshold, the HOMO ionization is always larger by about two orders of magnitude so that the contribution of the lower-lying orbitals is practically negligible as already noted, whereas the situation is quite different for  $N_2$ . Only at 200 nm ionization is dominated by the HOMO at all angles. At 266 nm again the  $1\pi_u$  becomes dominant at  $90^\circ$ , and at 400 nm it is  $2\sigma_u$ , which is comparable to  $3\sigma_g$  over a large angular region, and becomes even larger in a small region around its maximum at about  $75^\circ$ . This highly irregular behavior is quite unusual and probably reflects a resonance structure in both channels around 400 nm where a peculiar behavior is also clearly seen in Fig. 2 but only for the  $0^\circ$  and  $45^\circ$  orientations.

The use of a single-determinant approximation as the one adopted in this paper or as is the basis of time-dependent Hartree-Fock and density-functional approaches, appears to provide well-defined orbital-related observables. However, despite the fact that a single-determinant wave function is evidently an approximation to the true many-particle problem, an additional issue may arise due to the definition of the ionization yield from a given orbital. In this paper the ionization yield from orbital  $|\varphi_j\rangle$  is defined as the population of the (discretized) continuum states after propagating this orbital in the laser field, see Eq. (3). Within a frozen-core approximation this definition is well defined. However, in approaches in which all orbitals are simultaneously propagated in the light field, there is the possibility of a mixing among the (initially) occupied orbitals since a unitary rotation among occupied orbitals leaves the electron density unchanged. Particularly, for laser frequencies that are resonant with a transition among (initially) occupied orbitals, a real population transfer (after depopulation by ionization) or simply an orbital rotation may occur [2,20]. In the latter case, the definition of an orbital ionization yield becomes evidently questionable. For example, using time-dependent DFT in the calculation of the alignment-dependent ionization yield (at 800 nm) from the HOMO of molecular nitrogen [20,21], a distribution was found that deviates strongly from the orbital shape, whereas the total ion yield from all orbitals resembled the shape of the HOMO. Although the single-determinant approximation used in the present paper did not reproduce that result since the obtained alignment-dependent ionization yield (at 800 nm) of the HOMO orbital agrees in shape with the total ion yield [2], it is evidently an important question whether the pronounced structures in the wavelength scans shown here are, at least to a large extent, simply due to a rotation among occupied orbitals. In that case, the relevance of the orbital ionization yields would be less transparent since there would be no direct correspondence between the (observable) hole in the formed ion and the orbital ionization yield.

In order to investigate whether the structures in Figs. 2 and 3 are caused by orbital rotations or by REMPI and channel closings, Fig. 5 shows (as an example) the ionization and excitation yield of the initially propagated  $3\sigma_g$  orbital of  $N_2$

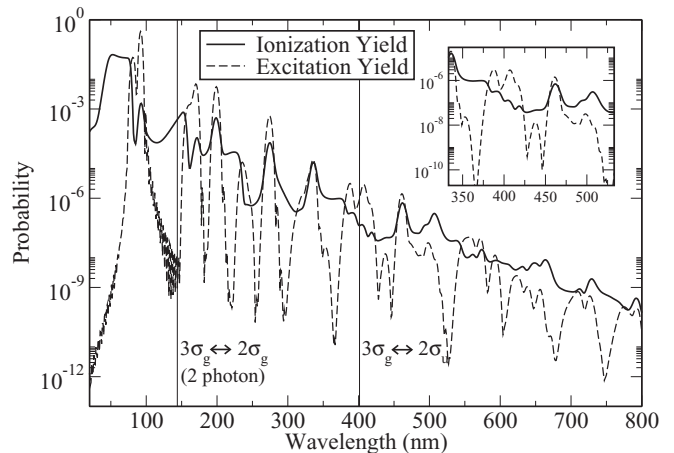


FIG. 5. Ionization and excitation yields of the  $3\sigma_g$  orbital of  $N_2$  as a function of the photon wavelength for parallel alignment. The laser parameters are the same as in Fig. 2. The position of the main resonant transitions with core orbitals (the one-photon coupling to the  $2\sigma_u$  orbital and the two-photon coupling to the  $2\sigma_g$  orbital) are indicated with vertical lines.

for parallel alignment. Similar to the ionization yield in Eq. (3) the excitation yield is defined as the sum over the populations of all initially unoccupied orbitals that possess, however, an energy below the ionization threshold. In REMPI processes, there is usually a substantial population of the intermediate excited state if the laser is not too strong and its duration not long enough that the intermediate state is fully ionized. Clearly, according to Fig. 5 most of the structures in the orbital ionization yields are accompanied by corresponding peaks in the excitation yield. This is clear proof that these structures are mainly due to REMPI processes. Most of the remaining structures can, on the other hand, be attributed to channel closings, see Fig. 2 for the corresponding thresholds. In Fig. 5 are also indicated the two dominant resonant wavelengths of the HOMO with other core orbitals. In particular, the one-photon resonance with the  $2\sigma_u$  orbital (at about 400 nm) should show a pronounced orbital coupling due to its transition-dipole strength but nevertheless leads to a negligible effect for the shown orbital ionization yield of the HOMO.

## V. SUMMARY AND CONCLUSIONS

An extensive survey of the ionization yields for the two molecules  $N_2$  and  $O_2$  over the wavelength range of 25–800 nm at the laser peak intensity of  $1 \times 10^{13} \text{ W/cm}^2$  has been performed. It is based on a numerical solution of the time-dependent Schrödinger equation employing a field-free static DFT Hamiltonian. This wavelength range is a region where molecular electronic structure is likely to be most important in the orbital ionization yields  $Y_j$  and in the photoelectron spectra and which has been little studied up to now in molecules because of a lack of suitable tunable sources. Both wavelength dependence and angular distributions have been reported, which show general trends superimposed with ubiquitous resonant structure, and the interplay of different ionizations, not only from the HOMO, in most of the region scanned. Therefore, a strong photon-energy dependence is

observed in both  $Y_j$  and relative orbital contribution as well as the angular distributions. As a consequence, results for a single frequency may not be representative of a general behavior in this energy-intensity region.

Despite limitations in the treatment of many-body effects in the present many-electron single-determinant approximation, previous experience makes one expect that a semiquantitative description of the general trends reported and, in particular, all qualitative features are generally realistic, although details of the resonant structures, more affected by the electron correlation neglected, may change in detail. It is expected that the results presented may be useful for the design of future experiments and will stimulate activity in this energy-intensity region. The exploration of a vast wavelength range has been possible due to the computational efficiency of the present

approach. It is clear that the full exploration of the three parameters wavelength, intensity and pulse duration, and shape or the behavior at constant values of other characteristic parameters, such  $U_p$ ,  $U_p/\omega$ , or  $\gamma$ , etc., will require a vast amount of computation, which is planned for future work.

#### ACKNOWLEDGMENTS

The authors would like to acknowledge the ITN COR-INF (Grant Agreement No. 264951, European Commission's Seventh Framework Programme), COST *XLIC* Action Grant No. CM1204, and COST Grant No. CM0702 for financial support. P.D. acknowledges financial support from CNR-INFN Democritos and the PRIN 2009 Project.

- 
- [1] D. Pavičić, K. F. Lee, D. M. Rayner, P. B. Corkum, and D. M. Villeneuve, *Phys. Rev. Lett.* **98**, 243001 (2007).
  - [2] S. Petretti, Y. V. Vanne, A. Saenz, A. Castro, and P. Decleva, *Phys. Rev. Lett.* **104**, 223001 (2010).
  - [3] S. Petretti, A. Saenz, A. Castro, and P. Decleva, *Chem. Phys.* **414**, 45 (2013).
  - [4] J. Itatani, J. Levesque, D. Zeidler, H. Niikura, H. Pépin, J. C. Kieffer, P. B. Corkum, and D. M. Villeneuve, *Nature (London)* **432**, 867 (2004).
  - [5] M. Meckel, D. Comtois, D. Zeidler, A. Staudte, D. Pavičić, H. C. Bandulet, H. Pépin, J. C. Kieffer, R. Dörner, D. M. Villeneuve *et al.*, *Science* **320**, 1478 (2008).
  - [6] Y. V. Vanne and A. Saenz, *J. Mod. Opt.* **55**, 2665 (2008).
  - [7] M. Awasthi, Y. V. Vanne, A. Saenz, A. Castro, and P. Decleva, *Phys. Rev. A* **77**, 063403 (2008).
  - [8] J. P. Farrell, S. Petretti, J. Förster, B. K. McFarland, L. S. Spector, Y. V. Vanne, P. Decleva, P. H. Bucksbaum, A. Saenz, and M. Gühr, *Phys. Rev. Lett.* **107**, 083001 (2011).
  - [9] R. van Leeuwen and E. J. Baerends, *Phys. Rev. A* **49**, 2421 (1994).
  - [10] D. Toffoli, M. Stener, G. Fronzoni, and P. Decleva, *Chem. Phys.* **276**, 25 (2002).
  - [11] K. P. Huber and G. Herzberg, *Molecular Spectra and Molecular Structure IV. Constants of Diatomic Molecules* (Van Nostrand-Reinhold, New York, 1979).
  - [12] B. K. McFarland, J. P. Farrell, P. H. Bucksbaum, and M. Gühr, *Science* **322**, 1232 (2008).
  - [13] H. Akagi, T. Otobe, A. Staudte, A. Shiner, F. Turner, R. Dörner, D. M. Villeneuve, and P. B. Corkum, *Science* **325**, 1364 (2009).
  - [14] O. Smirnova, Y. Mairesse, S. Patchkovskii, N. Dudovich, D. Villeneuve, P. Corkum, and M. Y. Ivanov, *Nature (London)* **460**, 972 (2009).
  - [15] H. R. Reiss, *Phys. Rev. A* **22**, 1786 (1980).
  - [16] P. Baltzer, M. Larsson, L. Karlsson, B. Wannberg, and M. Carlsson Göthe, *Phys. Rev. A* **46**, 5545 (1992).
  - [17] P. Baltzer, B. Wannberg, L. Karlsson, M. Carlsson Göthe, and M. Larsson, *Phys. Rev. A* **45**, 4374 (1992).
  - [18] K. Siegbahn, C. Nordling, G. Johansson, J. Hedman, P. F. Hedén, K. Hamrin, U. Gelius, T. Bergmark, L. O. Werme, R. Manne *et al.*, *ESCA Applied to Free Molecules* (North-Holland, Amsterdam/London, 1971).
  - [19] D. B. Milošević, *Phys. Rev. A* **74**, 063404 (2006).
  - [20] D. A. Telnov and S.-I. Chu, *Phys. Rev. A* **80**, 043412 (2009).
  - [21] D. A. Telnov and S.-I. Chu, *Phys. Rev. A* **79**, 041401(R) (2009).